ASTROBIOLOGY
Volume 6, Number 6, 2006
© Mary Ann Liebert, Inc.

Research Paper

Detectability of Planetary Characteristics in Disk-Averaged Spectra II: Synthetic Spectra and Light-Curves of Earth

GIOVANNA TINETTI,[1,2,3] VICTORIA S. MEADOWS,[1,4] DAVID CRISP,[1,5] NANCY Y. KIANG,[1,6] BRIAN H. KAHN,[5] EMMANUEL BOSC,[5] EVAN FISHBEIN,[5] THANGASAMY VELUSAMY,[1,5] and MARGARET TURNBULL[1,7]

ABSTRACT

Spatially and spectrally resolved models were used to explore the observational sensitivity to changes in atmospheric and surface properties and the detectability of surface biosignatures in the globally averaged spectra and light-curves of the Earth. Compared with previous efforts to characterize the Earth using disk-averaged models, a more comprehensive and realistic treatment of the surface and atmosphere was taken into account here. Our results are presented as a function of viewing geometry and phases at both visible/near-infrared (0.5–1.7 μm) and mid-infrared (5–25 μm) wavelength ranges, applicable to the proposed NASA-Terrestrial Planet Finder visible coronagraph and mid-infrared interferometer and to the ESA-Darwin mission architectures. Clouds can change the thermal emission by as much as 50% compared with the cloud-free case and increase the visible albedo by up to 500% for completely overcast cases at the dichotomy phase. Depending on the observed phase and their distribution and type, clouds can also significantly alter the spectral shape. Moreover, clouds impact the detectability of surface biosignatures in the visible wavelength range. Modeling the disk-averaged sensitivity to the "red-edge," a distinctive spectral signature of vegetation, showed that Earth's land vegetation could be seen in disk-averaged spectra, even with cloud cover, when the signal was averaged over the daily time scale. We found that vegetation is more readily discriminated from clouds at dichotomy (50% illumination) rather than at full phase. The detectability of phytoplankton was also explored, but was found to be more difficult to detect in the disk-average than land vegetation. Key Words: Radiative transfer—Remote sensing—Spectroscopy—Earth—Extrasolar terrestrial planets—Planetary science. Astrobiology 6, 881–900.

[1]NASA Astrobiology Institute; and [4]Spitzer Science Center and [5]Jet Propulsion Laboratory, California Institute of Technology, Pasadena, California.
[2]European Space Agency.
[3]Institut d'Astrophysique de Paris, Paris, France.
[6]NASA Goddard Institute for Space Studies, New York, New York.
[7]Carnegie Institution of Washington, Washington, DC.

INTRODUCTION

The first generation of extrasolar terrestrial planet detection and characterization missions—the NASA-Terrestrial Planet Finder (TPF) Coronagraph (TPF-C) and Interferometer (TPF-I) and the ESA-Darwin—will face a daunting technological challenge (Beichman *et al.*, 1999; Fridlung, 2000). The distances to the detector prohibit the ability to obtain spatial resolution on the extrasolar planet, and the relatively low brightness of the terrestrial-sized planet compared with its parent star severely limits both the spectral and temporal sampling of even the most interesting discovery.

The spectral information provided will be averaged over the observable disk and the exposure time, which may be hours or days, depending on the target. To determine planetary characteristics, we will need to interpret this space- and time-averaged information. Generally, because of the nature of the problem, the interpretation of the observed spectrum will not be unique, and a family of solutions will provide an equally good explanation of the spectral features. This expected degeneracy is due, in part, to a lack of spectral, spatial, and temporal sensitivity of these averaged spectra. Another source of degeneracy is given by space–time symmetries.

The current spectral resolutions proposed for TPF-C and TPF-I are $R = \lambda/\Delta\lambda \sim 70$ in the visible (VIS) and $R \sim 20$ in the mid-infrared (MIR), depending on the final architectures chosen. Figures 1 and 2 show realistic disk-averaged synthetic spectra of the Earth at the current nominal spectral resolving powers (R) for TPF-C and TPF-I and with a much higher resolution (1 cm^{-1}). At VIS wavelengths, $R = 70$ (Fig. 1) is high enough to discriminate O_2 and H_2O absorption in the Earth's spectrum, given sufficient signal-to-noise ratio (S/N). Discrimination of the O_3 Chappuis bands (0.5–0.7 μm) from the Rayleigh scattering shortward of 0.7 μm might be more problematic. In the MIR (Fig. 2), O_3 and CO_2 could be discriminated at $R = 20$, even with relatively poor S/N, but the peak in emission at the CO_2 line center due to the temperature inversion in the Earth's stratosphere requires much higher S/N to discriminate. Water vapor and CH_4 absorb at wavelengths between 6 and 8 μm, but the CH_4 absorption is difficult to discriminate at this resolving power.

Astrobiologists are interested in whether surface biosignatures studied by the Earth science remote sensing community could arise on an extrasolar planet and be detectable with TPF (Arnold *et al.*, 2002; Seager *et al.*, 2005). The red-edge, in particular, is a distinctive spectral signature of plants in the VIS: it begins between 0.68 μm and 0.7 μm and rises to a plateau at 0.761 μm. The low reflectance in the 0.45–0.52 μm (blue) spectral region is due to absorbance by carotenoids and chlorophylls; the one in the 0.63–0.7 μm (sometimes extending up to 0.73 μm) region is due only to chlorophyll, with the higher reflectance in the green responsible for the green color of most plants (Tucker, 1978).

Plankton also produces a distinctive surface signature (Kirk, 1983). The sunlight absorption that takes place in natural waters is attributable to the water itself, dissolved yellow pigments, the photosynthetic biota (phytoplankton and macrophytes), and inanimate particulate matter (tripton). Water absorption increases above 0.55 μm and is quite significant in the red region of the VIS. The general tendency is that, as phytoplankton concentration increases, reflectance decreases in the blue (0.4–0.515 μm) and increases in the green (0.515–0.6 μm). About 1% of the light a photosynthesizing cell absorbs is re-emitted as fluorescence, with a distinct peak at about 0.685 μm. Calculations indicate that the increased fluorescence associated with an increase in phytoplankton chlorophyll of 1 mg m^{-3} in the water would lead to an additional upward radiance of 0.03 W m^{-2} sr^{-1} μm^{-1} above the water (Kirk, 1983).

Previous work on characterizing the Earth using disk-averaged data uses both modeling and astronomical observing techniques of the disk-averaged Earth. Ford *et al.* (2001) developed a model by which to evaluate the photometric variability in specific bands in the optical (0.45, 0.55, 0.65, and 0.75 μm) due to daily rotation and seasons. Theoretical cloud-free light-curves of unresolved Earth in their model have variations of 10–20% with peaks of 100% when the ice amount is increased.

The model of Ford *et al.* (2001) predicts that clouds tend to raise the overall brightness and cloud patterns cause a variation of about 20% within a typical day if the planet is viewed from quadrature. Moreover, Ford *et al.* (2001) hypothesized that the diurnal rotational variation of an

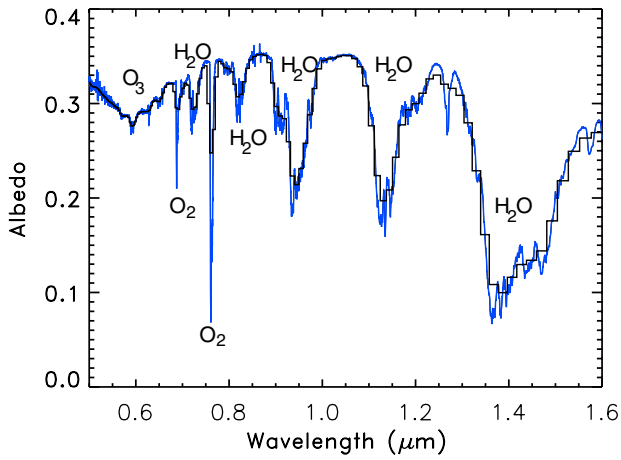

FIG. 1. Synthetic disk-averaged spectra of the Earth in the VIS-NIR, highly resolved (blue line) and at spectral resolution $R = 70$ (black line), simulating the TPF-C detection.

Earth-like planet is lower in the MIR (flux variation of a few percent). Their model accounts for different surface/cloud reflectivities, but does not include the contribution of an atmosphere.

Woolf *et al*. (2002) and Arnold *et al*. (2002) examined earthshine data (~0.4–0.9 μm) and derived the signature of Earth's vegetation. Woolf *et al*. (2002) identified the presence of oxygen, ozone, and water vapor in their earthshine spectrum, and made a preliminary identification of vegetation based on the enhancement of reflectivity redward of 0.73 μm. Arnold *et al*. (2002) used the relative contribution between the reflected fluxes in the broad red and infrared bands to quantify the vegetation signature in a sample of earthshine spectra. They concluded that the Earth's vegetation signature might be seen, but it is difficult to measure in the earthshine because of variable cloud cover, phase, and strong atmospheric bands absorbing in the red-edge wavelength range. In a more recent paper, Arnold *et al*. (2003) used the Earth daily maps acquired by the POLDER-1 satellite to compute their vegetation index for different simulated phases and observed latitudes.

In this paper, we build on this pioneering work by using a comprehensive model that incorporates the presence of the surface, atmosphere, and realistic clouds and is able to simulate cases not available from the observational data sets. In a previous paper (Tinetti *et al*., 2006a), we described the details of the model and its validation against observations of the Earth in the MIR, near-infrared (NIR), and VIS wavelengths.

To understand the detectability of Earth's global characteristics in the disk-average, we have studied the sensitivity of disk-averaged spectra to viewing geometries, phases, cloud cover, and surface signatures (*e.g*., ocean, ice, land/marine vegetation). Light-curves, obtained by integrating the spectral signal over a specific band, were also simulated.

Our previous work (Tinetti *et al*., 2006a) showed that clouds can substantially alter the intensities and shape of the Earth's disk-averaged spectra by masking, reducing, or enhancing some atmospheric features, depending on cloud altitude, composition, and optical depth (Kuze and Chance, 1994). Here, we show some specific examples to quantify cloud contributions as a function of phase, type, and distribution. As one might expect, our ability to detect surface biosignatures in disk-averaged spectra depends strongly on the spatial extent of vegetation and the fraction that is obscured by clouds. In addition, although Earth-observing techniques exist for the detection of vegetation in clear-sky cases over a limited portion of the planet, these techniques are not necessarily applicable to disk-averaged spectra. We report here the selection of spectral bands to be used as indicators of photosynthetic activity in the disk-average and discuss their sensitivity to the illuminated phase and cloud cover. Finally, we explore the effects of

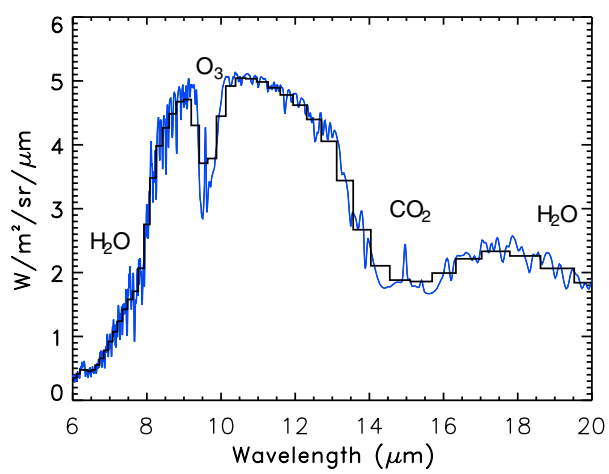

FIG. 2. Synthetic disk-averaged spectra of the Earth in the MIR, highly resolved (blue line) and at spectral resolution $R = 20$ (black line), simulating the TPF-I detection.

daily rotation and time averaging over the diurnal cycle for a couple of phases, with and without the contribution of clouds. These results have implications for TPF and Darwin, since these instruments will probably require integration times of several days or weeks to provide adequate S/N to detect biosignatures.

MODELING AND ANALYSIS

To assess detectability of planetary characteristics in disk-averaged spectra, we used a radiative transfer algorithm to generate high spectral resolution synthetic radiances for a global three-dimensional model of the Earth's atmosphere and surface. Results from this model were then averaged over the disk to yield a disk-averaged spectrum of the planet. Tinetti *et al*. (2005) have provided a detailed description of the physics of the planetary model, and Tinetti *et al*. (2006a) have provided further information on the datasets used in the creation of the Earth model. In subsequent sections, we explain how we calculated the broad-band integrated fluxes, and we define the indicators we used to quantify the relative photometric contributions of two selected bands. These quantities were used to generate light-curves or to discriminate the presence of clouds versus surface biosignatures.

Synthetic spectral datasets

We have generated with our model a variety of disk-averaged (and time-averaged in some particular cases) synthetic spectra and light-curves. These tools have been used for simulations of an increasing cloudy/forested/oceanic/icy Earth (see Effects of surface types and clouds) and to quantify the spectral variability at VIS, NIR, and MIR wavelengths as a function of the viewing angle (from north and south poles, and from equator spotting at the planet while it is rotating; see Sensitivity to viewing geometries, Light-curves, and Detectability of surface biosignatures), phases (fully illuminated, gibbous, dichotomy, and crescent; see Sensitivity to phase and Light-curves), and cloud cover (clear-sky, completely overcast, and using satellite data for realistic distributions). Finally, we performed experiments to determine the detectability of biosignatures on an Earth-like planet (red-edge signal and presence of plankton). In particular, in Detectability of surface biosignatures, we have examined the sensitivity of the red-edge detectability to varying (1) planetary geometric views (changes in observed land cover), (2) clouds (effect of cloud type, area covered, and distribution) over the present-day Earth's surface, (3) phase of the observation, and (4) the concentration of chlorophyll in phytoplankton.

Calculating light-curves

Time-dependent variations in the disk-averaged spectra, or "light-curves," can provide additional information about spatial variations in the surface and atmosphere of a planet even if it is unresolved. To quantify the change in broad-band albedo (VIS and NIR) and thermal emission (MIR) as either a function of the illuminated phase or the diurnal rotation of the planet at a fixed phase, the broad band integrated flux is calculated as:

$$\frac{\int_{\lambda_1}^{\lambda_2} I\, d\lambda}{\int_{\lambda_1}^{\lambda_2} d\lambda} \tag{1}$$

where $I(\lambda)$ is the disk-averaged albedo or emitted radiation, and λ_1 and λ_2 are the extremes of the chosen band interval. At fixed phase (here, we selected the half-illuminated and totally illuminated cases), we generated light-curves for 0.5–0.55 μm and 0.74–0.75 μm for the VIS and 8–13 μm for the MIR.

To quantify the variation in shape of cloudy disk-averaged spectra as a function of phase, we determined the relative photometric contribution of two selected bands in the VIS, paralleling a similar technique used in Earth remote sensing to discriminate vegetation:

$$\text{Normalized difference albedo index} = \frac{A - B}{A + B} \tag{2}$$

Here, we used 0.5–0.55 μm for the B band and 0.84–0.89 μm for the A band. In the cloud-free case, this index is sensitive to the relative contribution of different surface types, especially ocean versus vegetation.

Normalized difference vegetation index (NDVI)

The grass and forest albedo curves in Fig. 3 illustrate the red-edge. To quantify the strength

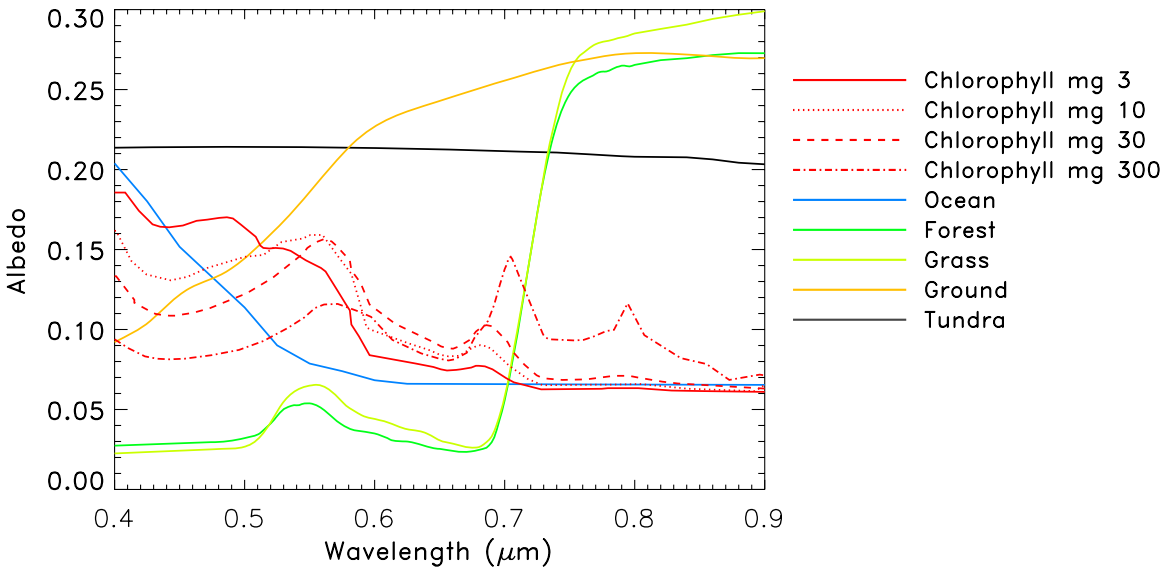

FIG. 3. Reflectance in the optical/NIR for nine of the 10 surface types used in our model: sterile ocean (blue line), forest (dark green line), grass (light green line), tundra (black line), and desert (yellow line). The red lines show ocean with plankton in different concentrations (from 5 to 300 mg/m^3). For a present-day Earth, the average concentration hovers between 0.1 and 10 mg/m^3, with peaks up to 30 mg/m^3. Ice reflectance has not been included in this plot since it would be out of range (~0.8 in the chosen wavelength window).

(hence the potential detectability) of the vegetation "red-edge," we used a commonly used index of vegetation activity—the NDVI—which is a measure of the contrast between the red and NIR reflectances. A high NDVI is correlated with high absorbance and air spaces in leaves. Note that NDVI is an indicator of photosynthetic activity, but its use in any actual quantification of photosynthesis is only correlative because many other vegetation features (*e.g.*, canopy structure, leaf surface characteristics) can cause variation in NDVI (Kiang *et al.*, 2006). Nonetheless, it is a useful photosynthetic activity indicator. NDVI is calculated as:

$$NDVI = \frac{NIR - R}{NIR + R} \tag{3}$$

where *NIR* is near-infrared reflectance, and *R* is red light reflectance.

The choice of bands for calculating NDVI varies among different workers depending on available data. Landsat Thematic Mapper sensors have bands at 0.63–0.69 μm and 0.74–1.10 μm for the red and NIR, respectively (Tucker, 1978). The National Oceanic and Atmospheric Administration uses bands at 0.58–0.68 μm and 0.725–1 μm for the VIS and NIR, respectively. The Earth Observing System Moderate Resolution Imaging Spectroradiometer sensors, designed to avoid windows of atmospheric absorbance for bands specific to surface remote sensing, detect the red band at 0.649–0.679 μm and an NIR band at 0.855–0.875 μm (Salomonson and Toll, 1991). These ranges are not affected by atmospheric absorbance due to O_2 and H_2O vapor. Arnold *et al.* (2002) selected bands at 0.6–0.67 μm for the red and 0.74–0.8 μm for the NIR to quantify the vegetation signature in the earthshine spectra.

Here, we calculated the disk-averaged NDVI of our model using 0.65–0.68 μm for the red and 0.74–0.8 μm for the NIR. We have explored also the possible use of alternative bands for our model; the final selection was driven above all by the sensitivity of those bands to the presence of clouds (see Discussion).

Cloud distribution and optical properties

In this investigation, top and bottom pressures, the optical depths for each cloud type (low, medium, and high), and the cloud fractional coverage at the daily scale were taken from Atmospheric Infrared Sounder (AIRS) Level 2 Simulation System (Fishbein *et al.*, 2003). The wavelength-dependent optical properties for liquid water clouds were generated using Mie scattering, while the optical properties for cirrus ice clouds were generated using geometric optics (*cf.* Crisp, 1997).

From the satellite perspective, we used the International Satellite Cloud Climatology Project (ISCCP) (Rossow and Schiffer, 1999) cloud climatology (1983–2001) in conjunction with the AIRS (Aumann *et al*., 2003) to arrive at a representative global cloud field and discuss annual, seasonal, and monthly averaged distributions for low, medium, and high clouds.

Surface albedo signatures

As in Tinetti *et al*. (2006a), the land surface was classified into one of six distinct surface cover types (ocean, forest, grass, tundra, rock, and ice). The wavelength-dependent albedos for each type were derived from the ASTER Spectral Library (see: http://speclib.jpl.nasa.gov/) (Gower *et al*., 2004). In addition, here we have modified the ocean albedos by adding variable amounts of plankton. At VIS wavelengths, the reflectance spectra of the ocean with plankton at increasing concentrations were taken from Gower *et al*. (2004) and Kirk (1983) (Fig. 3).

RESULTS

Effects of surface types and clouds

To assess the contributions of the various surface cover types, we ran simulations covering the Earth with one surface type at a time. Figure 3 shows the measured surface reflectances used as input in our simulations. Figure 4 shows disk-averaged spectra of ocean (dark blue lines), ice (black dotted lines), forest (darker green lines), grass (green lines), and tundra (black solid lines) worlds. The viewing geometry and illumination were the same in each of the plots, *i.e*., with the observer looking at the half-illuminated planet from over the equator. In the MIR, it was impossible to distinguish among the different surface types (Fig. 4a) because the surface reflectance in that wavelength range was uniformly low and did not change appreciably. The opposite was true in the VIS/NIR (Fig. 4b and c).

The light blue lines in Fig. 4 show the contribution of the different cloud types—cirrus (dash-dotted line), altostratus (dashed line), and stratocumulus (dotted line). As shown in Fig. 4b, an enlargement of the 0.7–0.8 μm band where the red-edge signal is detectable, leafy plants reflect sunlight strongly in these wavelengths. The red-edge detectability is discussed subsequently.

Sensitivity to viewing geometries

Disk-averaged VIS, NIR, and MIR spectra of the Earth were generated from several vantage points (*i.e*., over the pole, over the equator, etc.) with the same illumination (Fig. 5). In particular, Fig. 5 shows synthetic spectra for a fully illuminated disk for a day in northern hemisphere summer. In the VIS/NIR, with a cloud-free sky (Fig. 5a), the main differences among the spectra were due to changing surface cover type. For this season, the southern polar cap was more extended (ice has a very high reflectance in the VIS/NIR; Fig. 4c) and the northern hemisphere more forest-covered.

Differences between the two equatorial viewing geometries were due to the presence of more land/vegetation in one case (longitude 0°) and more ocean in the other (longitude 180°). Both the north pole and the equator longitude 0° cases simulate viewing geometries that included a large amount of vegetation. The green and light blue plots show a very distinct red-edge signal starting from 0.7 μm. When clouds were included with realistic fractional coverage (Fig. 5b), the albedo was substantially higher, and differences among the four cases were reduced. In Fig. 5b, the most ice-covered disk-averaged spectrum still maintained the highest albedo, though it was not possible to distinguish whether this is due to high clouds or surface ice. The red-edge signal was still perceivable, by inspection, at least for the view from the north pole (see Detectability of surface biosignatures for a longer discussion about the red-edge and NDVI).

In the NIR, for a cloud-free sky (Fig. 5c), the presence of ice (see Fig. 4c) for the polar view (gray plot) was particularly prominent in the 1.4–1.5 μm band. When clouds were accounted for (Fig. 5d), the albedo increased in the NIR as well. The presence, and sometimes even type, of clouds could be discriminated as a result of differences in the water/ice absorption bands around ~1.4 and ~1.9 μm.

In the MIR (Fig. 5e), the observed variations were due to the pole-to-pole temperature gradients. As we expected because of the time of the year, the lowest average temperatures were seen for the south pole view. The presence of clouds lowered the average emitting temperature and

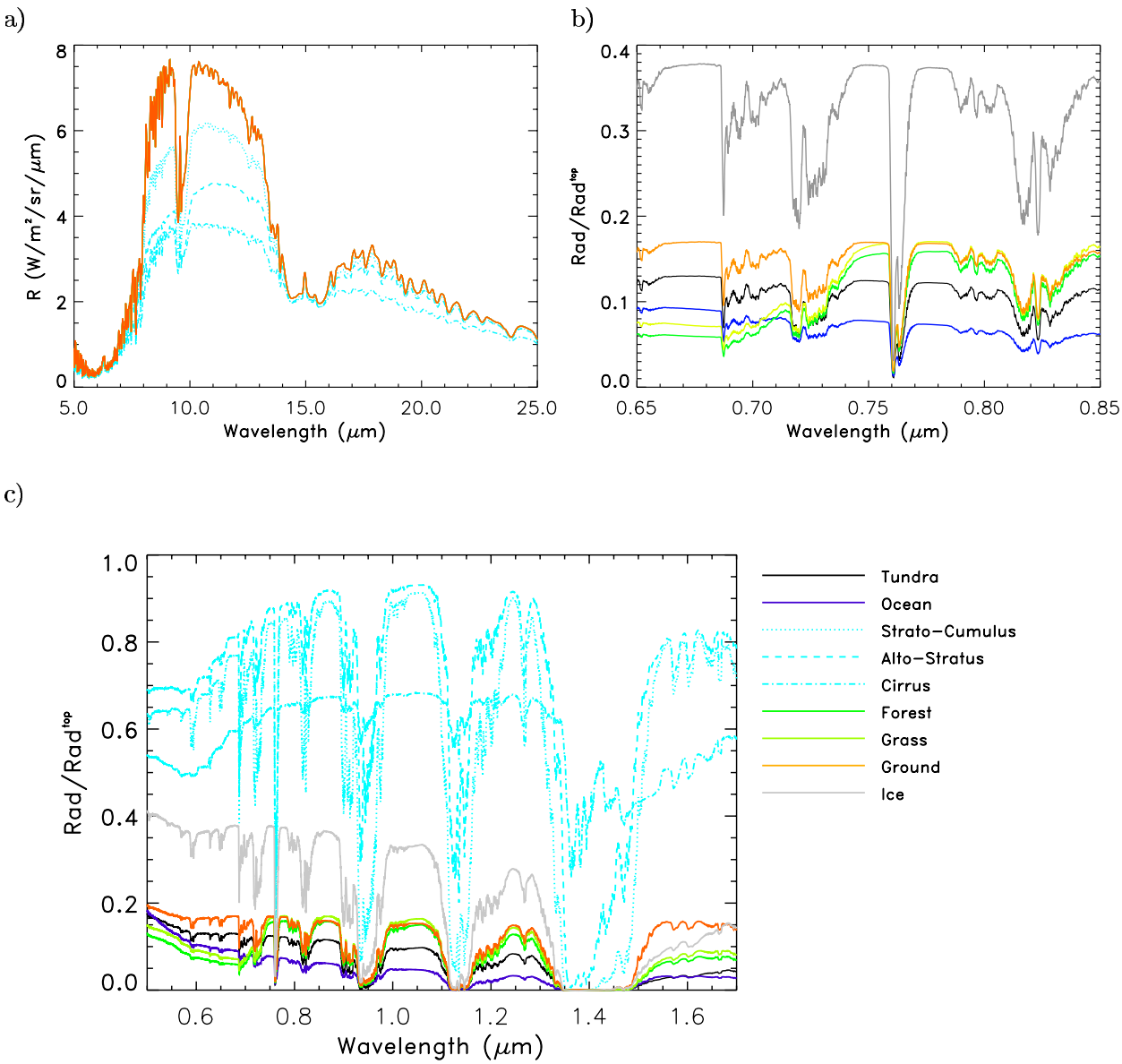

FIG. 4. Disk-averaged spectra with single surface type coverage (blue line, ocean; dotted black line, ice; yellow line, desert; green line, vegetation; solid black line, tundra). Note the pronounced differences in the VIS-NIR (**b** and **c**) spectra, whereas differences are minimized in the infrared (**a**) spectra. Light blue plots show the contribution of clouds: cirrus (dash-dotted line), altostratus (dashed line), and stratocumulus (dotted line). The red-edge signal due to the strong reflectance of leafy plants is visible in the 0.7–0.8 μm band.

masked the latitudinal temperature gradients (Fig. 5f).

Sensitivity to phase

We performed experiments to explore the sensitivity of disk-averaged spectra to different illuminated phases. No pronounced differences were seen in the MIR, except those caused by changes in the temperature/cloud vertical distribution (~6% for the cloud-free case and ~12% for the low-cloud case; compare the four plots in Fig. 6, right column).

Figure 6 shows the results for the VIS/NIR (center column). For the cloud-free disk-averaged spectra (black lines), there were only small differences in the VIS/NIR albedo among the four cases. In contrast, dramatic changes were observed for the fully cloud-covered disk-averaged spectra (light blue, cirrus; blue, altostratus; vio-

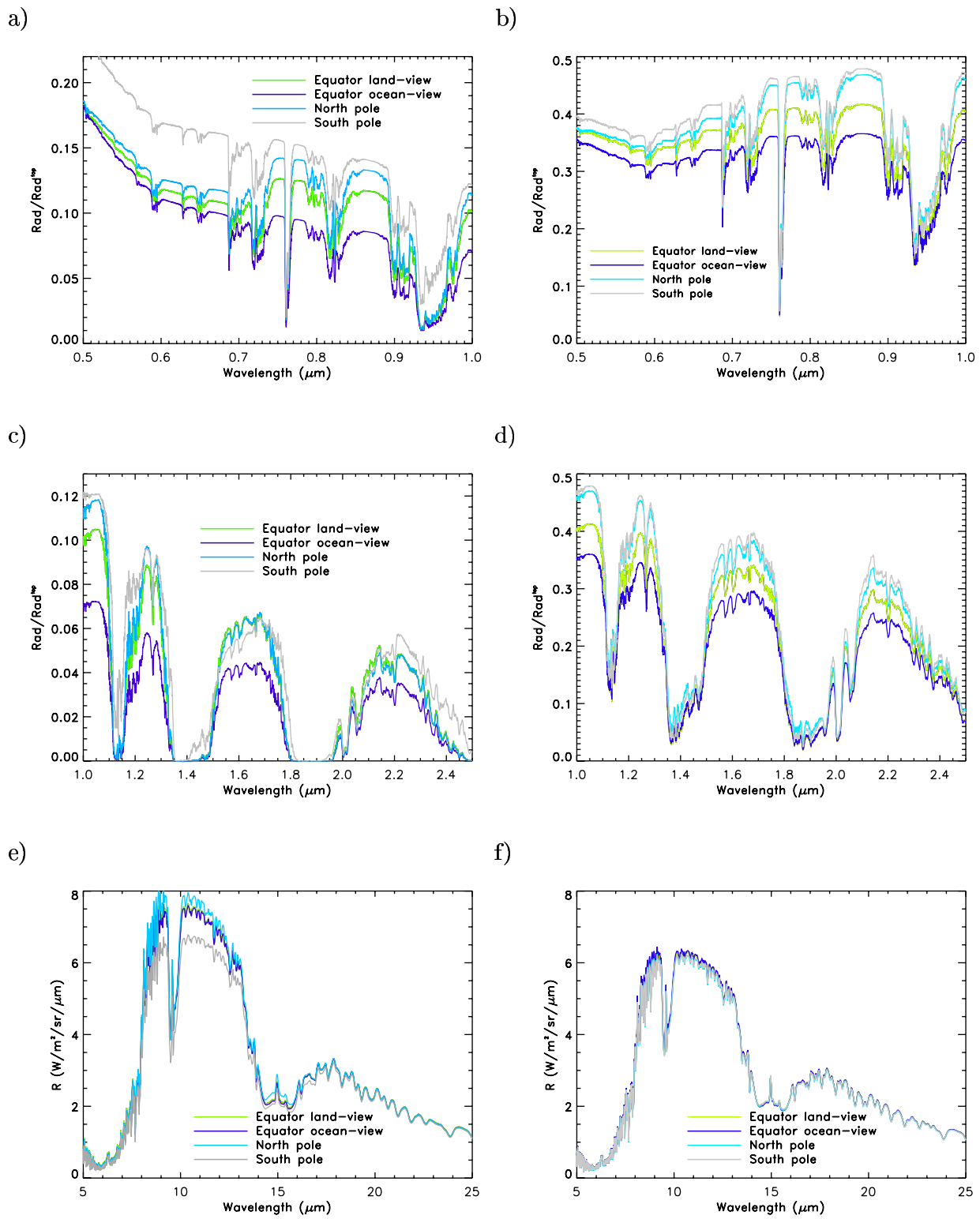

FIG. 5. Earth VIS (a and b), NIR (c and d), and MIR (e and f) disk-averaged spectra: (a, c, and e) cloud-free cases and (b, d, and f) monthly average distribution of clouds (ISCCP data products). AIRS data corresponding to July 2002 were used as input to the model. Viewing positions are as follows: light blue line, north pole; gray line, south pole; green line, equator land-view; dark blue line, equator ocean-view.

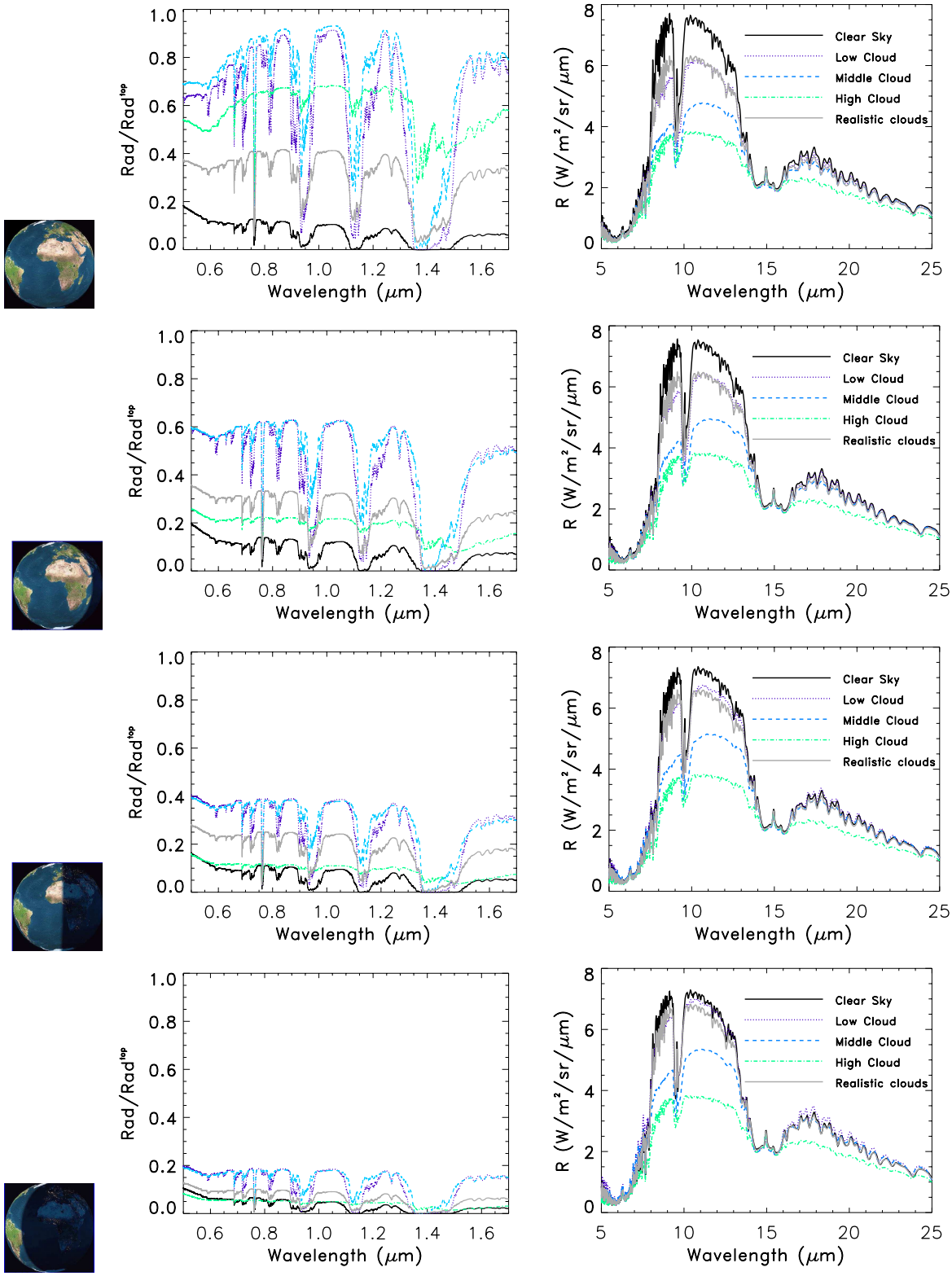

FIG. 6. Disk-averaged spectra of the Earth in the VIS-NIR (center column) and in the MIR (right column) relative to the four different phases (left column). Solid black lines, cloud-free disk-averaged spectra; gray line, realistic nonuniform cloud coverage; blue dashed/dotted lines, completely overcast (dot-dashed light blue line, cirrus; dashed blue line, altostratus; dotted violet, stratocumulus).

let, stratocumulus) and the realistic cloudy case (gray lines), which used the spatial distribution of clouds from the ISCCP/AIRS dataset. Differences were noted in both the amplitude and the spectral shape of the albedo (see Fig. 7 for a photometric quantification of both of these effects). This behavior was mostly due to variations in the atmospheric pathlength above the clouds. When the observable disk was fully illuminated, the observer and the Sun were at the same position, and the full disk spectrum included the full-range solar zenith angles and emission angle between 0° and 90°. For this geometry, the brightening associated with Rayleigh scattering at the blue end of the VIS spectrum was suppressed in cloudy conditions because the Rayleigh scattering optical depth is proportional to the atmospheric pressure and clouds limited the observed column to that above their tops. Reductions in the optical pathlength by clouds also reduced the absorption by molecular oxygen and water vapor at longer wavelengths (*i.e.*, the centers of the bands were no longer completely black). High clouds reduced the absorption by water vapor more than that of oxygen since the water vapor was concentrated near the surface, while oxygen was mixed uniformly through the column. The absorption by ozone at the blue end of the spectrum was not reduced substantially by clouds because the majority of the ozone was in the stratosphere above the cloud tops.

As the illuminated phase was decreased from full phase (100%) to dichotomy (50%), the solar and emission zenith angles increased, which resulted in longer optical paths above the cloud tops. In the crescent phase, all solar zenith and emission angles were near 90°. For these long pathlengths, the Rayleigh scattering optical depth at the blue end of the spectrum was much larger than unity even in the presence of high clouds, and the relative contributions by ozone and Rayleigh scattering to the spectrum were similar to those observed in the cloud-free case.

Light-curves

Time-dependent variations in the disk-averaged spectra, or "light-curves," also varied with the illuminated phase of a planet. Figure 7a shows the broad-band photometric variability for the spectral interval extending from 0.5 to 0.9 μm as a function of phase (Eq. 1). The cloudy cases brightened most near 0 and 2π phase, as shown in the previous section. The uniformly overcast cases (stratocumulus, altostratus, and cirrus) showed an expected symmetry of the curves with respect to the π phase (*i.e.*, totally dark point). In contrast, the case with the realistic cloud distribution was slightly asymmetric about this point because of changes in the cloud pattern.

Figure 7b shows the relative photometric contribution of two selected bands in the VIS, 0.5–0.55 and 0.84–0.89 μm, as a function of phase. This is another way of showing how the disk-averaged spectral shape changed from a fully illuminated to a totally dark phase. The relative photometric contribution was defined by Eq. 2 in Calculating light-curves. When this indicator was negative, we had a pronounced contribution in the disk-averaged spectra by Rayleigh scattering. In a cloud-free case, this contribution was always negative, but changed depending on the distribution of land and vegetation versus ocean (cloud-free ocean cases always show a very negative value for this index). For cirrus clouds and clouds realistically distributed, the index progressively decreased from positive values for the totally illuminated phase to negative values as the totally dark phase, which is a singularity, was approached. For low and middle clouds (*e.g.*, stratocumulus and altostratus), the index was always positive and reached a minimum near 0 at dichotomy. This behavior created some problems for distinguishing the contribution of vegetation from clouds, as discussed in more detail in the following sections.

Figure 8 shows rotational light-curves at constant phase (Eq. 1) for two different phases, dichotomy (gray lines) and totally illuminated (black lines), following the diurnal rotation of the planet. Figure 8a shows the spectral interval 8–13 μm. Although the daily periodicity associated with albedo differences between the oceans and continents was clearly seen in both clear-sky curves, variations in the flux during the rotation in this spectral range was only 3–4% for the fully illuminated disk and dichotomy. It is unlikely that the first generation of space-based extrasolar terrestrial planet observatories will be sensitive enough to detect such subtle fluctuations. The relatively small longitudinal gradients in the MIR radiances were due to the presence of a thick atmosphere, which moderates the temperature differences between the oceans and the land. When

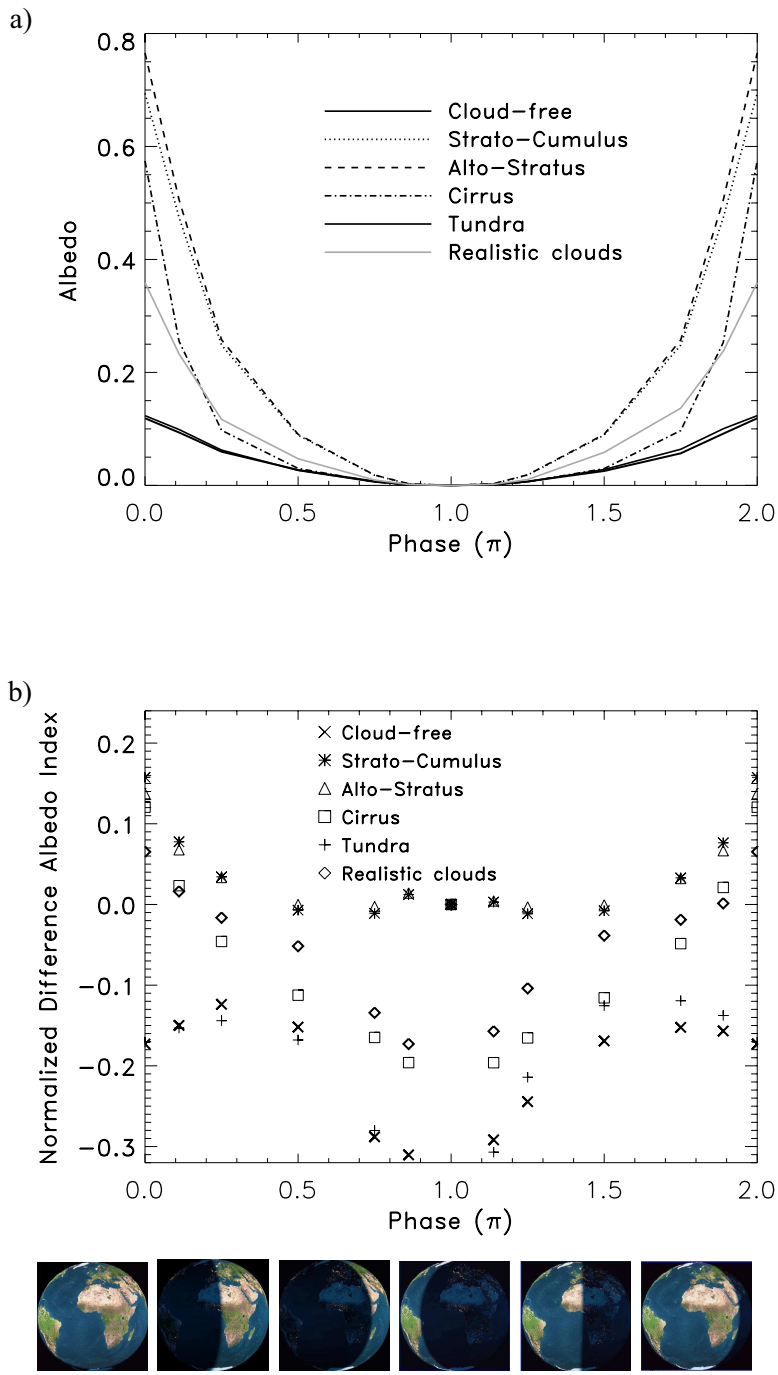

FIG. 7. (**a**) Phase light-curves for the spectral band 0.5–0.9 μm. (**b**) Phase light-curves showing the relative photometric contribution of two selected bands in the visible (0.5–0.55 μm and 0.84–0.89 μm). Phases = $0 \approx 2\pi$ correspond to the fully illuminated disk, phase = π (a singularity) to the totally dark. **Bottom panel:** Some of the phases used in (a) and (b): 0, $\pi/2$, $3\pi/4$, $5\pi/4$, $3\pi/2$, and $7\pi/4$.

clouds were added [we chose the distribution for a particular day in July (Fishbein *et al.*, 2003)], the fluctuations due to different cloud distributions did not increase substantially, but the daily periodicity was lost.

Figure 8b shows albedo light-curves for bands centered between 0.5 and 0.55 μm. These light curves showed less than 10% variability. By contrast, a band that extended from 0.74 to 0.75 μm showed higher modulation because of the presence of the red-edge signal (40–50% variability), as discussed further in the next section. When clouds were included, the albedo increased 100% (dichotomy) and 200–300% (fully illuminated disk). The band-weighted integrated flux showed fluctuations of 50% (dichotomy) and 25% (fully illuminated disk). Interestingly, as the phase changes, the two bands switched their relative

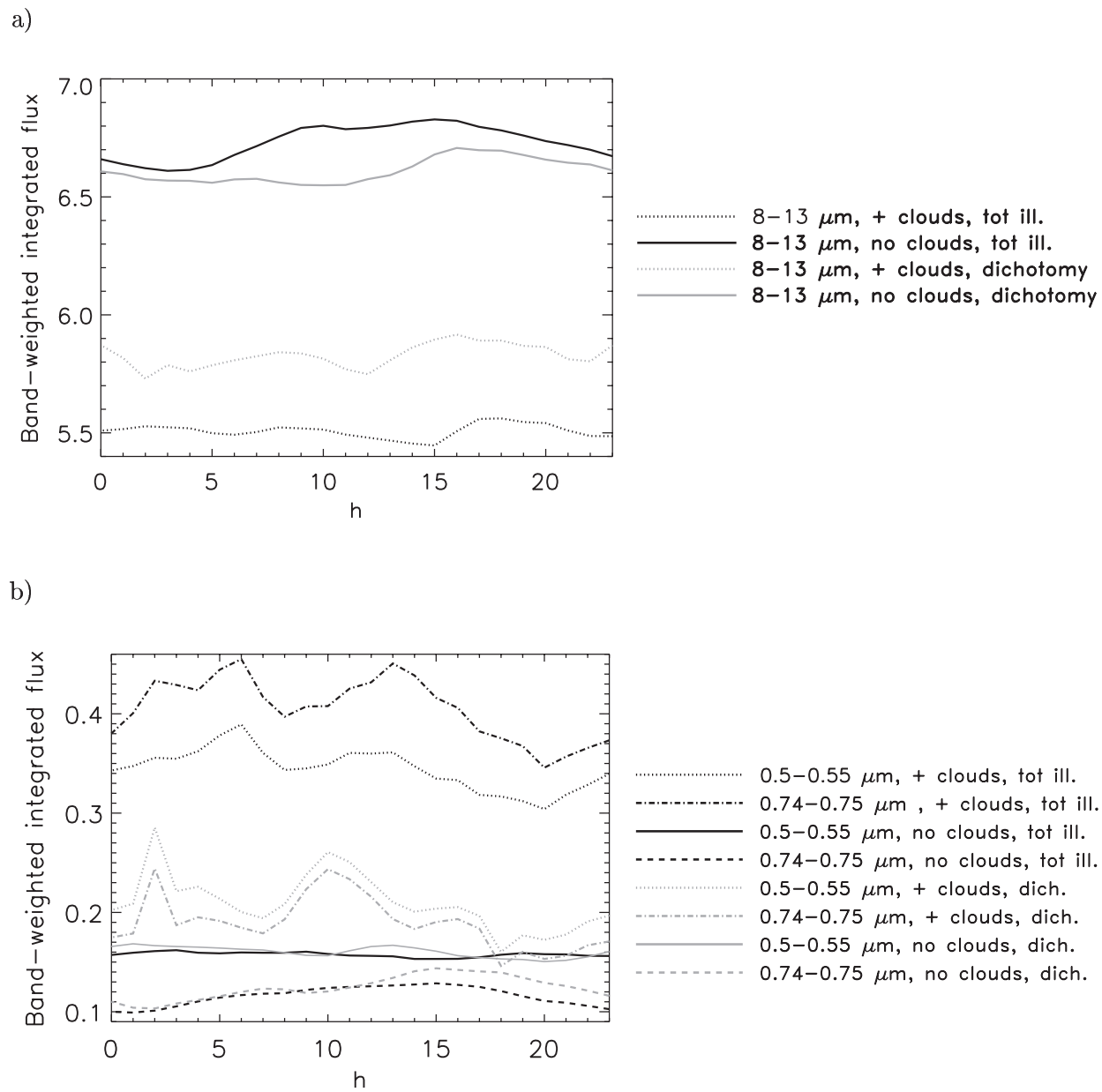

FIG. 8. Light-curves at constant phase, fully illuminated (black lines) and dichotomies (gray lines) following the diurnal rotation of the planet, for a cloud-free and a cloudy Earth. We assumed the cloud distribution of a particular day in July. (**a**) Infrared. Integrated flux in the spectral band 8–13 μm. (**b**) VIS. Integrated spectra in the spectral bands 0.5–0.55 μm and 0.74–0.75 μm. In both these plots the observer is positioned close to the equator.

contribution, which confirmed the predictions illustrated in Figs. 6 and 7b.

Detectability of surface biosignatures

In Sensitivity to phase, we defined the NDVI (Eq. 3) and selected 0.65–0.68 μm for the red band and 0.74–0.8 μm for the NIR band. The rationale for this final selection was the result of an extensive exploration of alternative bands, especially for the NIR, *e.g.*, 0.855–0.875 μm or a band wider/narrower than the chosen 0.74–0.8 μm. As explained in Discussion, this choice optimized several parameters.

When we calculated the NDVI for a planet entirely covered by a single surface type (Fig. 4c) and for different phases (100%, 75%, 50%, and 25% of the disk illuminated), we obtained the results shown in Table 1.

In a clear-sky case, the only surface that

TABLE 1. VALUES OF NDVI FOR DIFFERENT SURFACE AND CLOUD TYPES, FOR FULLY ILLUMINATED, GIBBOUS, DICHOTOMY, AND CRESCENT PHASES

	NDVI			
Surface type	*Fully illuminated disk*	*Gibbous*	*Dichotomy*	*Crescent*
Ocean	−0.15	−0.16	−0.16	−0.14
Tundra	−0.08	−0.07	−0.07	−0.07
Desert	−0.05	−0.05	−0.05	−0.04
Ice	−0.05	−0.04	−0.04	−0.04
Low (stratus)	8.10^{-3}	−0.03	−0.03	−0.02
Medium (cumulus)	0.01	−0.02	−0.02	−0.02
High (cirrus)	0.03	−0.04	−0.03	−0.02
Grass	0.34	0.3	0.3	0.38
Forest	0.4	0.42	0.42	0.47

For all the phases, in the clear sky case, only vegetation had a positive NDVI.

showed a positive NDVI was vegetation. Clouds only produced a positive NDVI for phases close to fully illuminated (*i.e.*, the albedo intensity was maximum, and the shape mimicked closely the red-edge; see also Sensitivity to phase and Fig. 6), which will not be observed by TPF or similar future missions. For all the other phases, we kept "0" as the threshold to discriminate the presence of land photosynthetic activity.

Red-edge signal and clouds

Figure 9a shows synthetic disk-averaged spectra between 0.6 and 0.95 μm for different views of a cloud-free, half-illuminated Earth over a diurnal cycle. The NIR reflectance by vegetation was responsible for ~50% of the variation in the signal. Land vegetation on Earth produced a strong, disk-averaged red-edge feature when there were no clouds. Although the initial rise of the red-edge at around 0.68 μm was obscured by atmospheric water vapor absorption, the latter part of the red-edge was captured by the rise in the 0.73–0.81 μm range. The plateau at 0.745 μm occurred earlier than the actual vegetation red-edge plateau at 0.76 μm due to atmospheric water vapor. For cloud-free cases, the red-edge could not be discriminated when the Pacific Ocean dominated the view. The peak detectability (~40–50%) occurred in cloud-free cases where Africa and the Eurasian continents occupied most of the observable half-hemisphere. When clouds were included (Fig. 9b), it became harder to discriminate by inspection the red-edge, but it was possible using vegetation indicators.

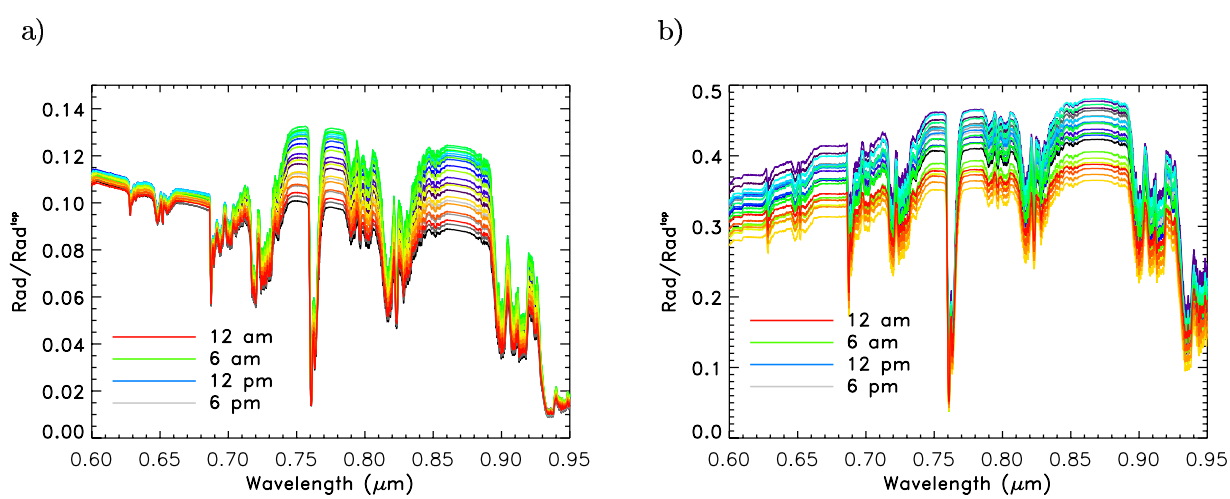

FIG. 9. Disk-averaged spectra in the optical of a half-illuminated cloud-free Earth (a) and a cloudy Earth (b) seen from different views following the diurnal rotation of the planet. The land versus ocean fraction changes considerably with time.

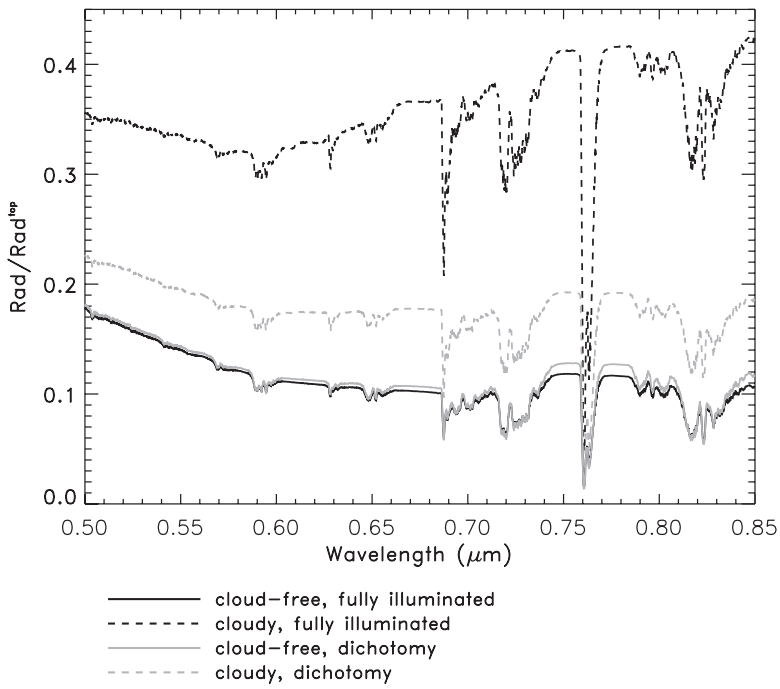

FIG. 10. Time-disk averaged spectra of the Earth: daily average of a cloud-free (solid lines) and a cloudy (dashed lines) Earth in the optical. Black lines, fully illuminated disk; gray lines, dichotomies. NDVI values calculated for these time-disk averaged cases are as follows: 0.013 and 0.029 (cloud-free; fully illuminated and dichotomy, respectively) and 0.025 and ~0 (cloudy; fully illuminated and dichotomy, respectively). According to these NDVI values, the red-edge is still observable for both the clear-sky cases and the cloudy dichotomy; an ambiguous situation exists for the cloudy, fully illuminated case.

We integrated the spectra shown in Fig. 9a and b over the diurnal time scale for a disk at dichotomy and at full phase (Fig. 10). In the cloud-free cases (solid lines), land surface vegetation produced a detectable disk-averaged signal for the red-edge, even when we averaged over the diurnal cycle. This conclusion was confirmed by NDVI, which was positive for both phases. In the cloudy cases (dashed lines), the index was close to 0 for dichotomy, which indicated the presence of vegetation. For the fully illuminated case, it had a positive value below 0.03, the value calculated for cirrus clouds (Table 1); thus the vegetation signature was ambiguous. This information could be useful for a mission like TPF-C, which will probably require integration times of the order of a day.

Figure 11 shows the sensitivity of NDVI to different views of the Earth with and without cloud cover (clear sky, black solid lines; cloudy, black dashed lines) and two phases [dichotomy (Fig. 11a) and fully illuminated (Fig. 11b)]. When we included clouds (nonuniformly distributed) for both phases, the red-edge detectability was progressively reduced. Considering the values in Table 1, we inferred that vegetation was present when NDVI was positive (gray solid line, threshold), except for the fully illuminated cloudy case, for which the threshold needed to exceed 0.03 (gray dashed line).

Figure 12 shows the sensitivity of the disk-averaged and diurnally averaged spectra to percent cloud cover and to land versus ocean cover. The clouds, incremented from cloud-free to 100%, were simulated only over the part of the surface covered by vegetation. The dotted curve represents a simulation with land vegetation completely replaced by cloud-free ocean.

Plankton

Plankton also features a red-edge, though it is harder to detect than that of land plants. Figure 13 shows disk-averaged spectra of an ocean view of Earth, with an increasing concentration of plankton. This was an "optimistic" result, meaning that the spectra are cloud-free and the viewing geometry and season were optimized so that plankton could be detected (see: http://seawifs.gsfc.nasa.gov/SEAWIFS.html). Figure 14 shows the results obtained when we increased the concentration of plankton and compared our results with the earthshine spectrum recorded by Woolf *et al*. (2002) (Tinetti *et al*., 2006a). When clouds were included in the simulations, as in this specific case, the presence of plankton was more difficult to detect. Though we did not expect to have much plankton (~3 mg/m^3) to be present during the month of the year when earthshine was recorded (June), we found that adding the con-

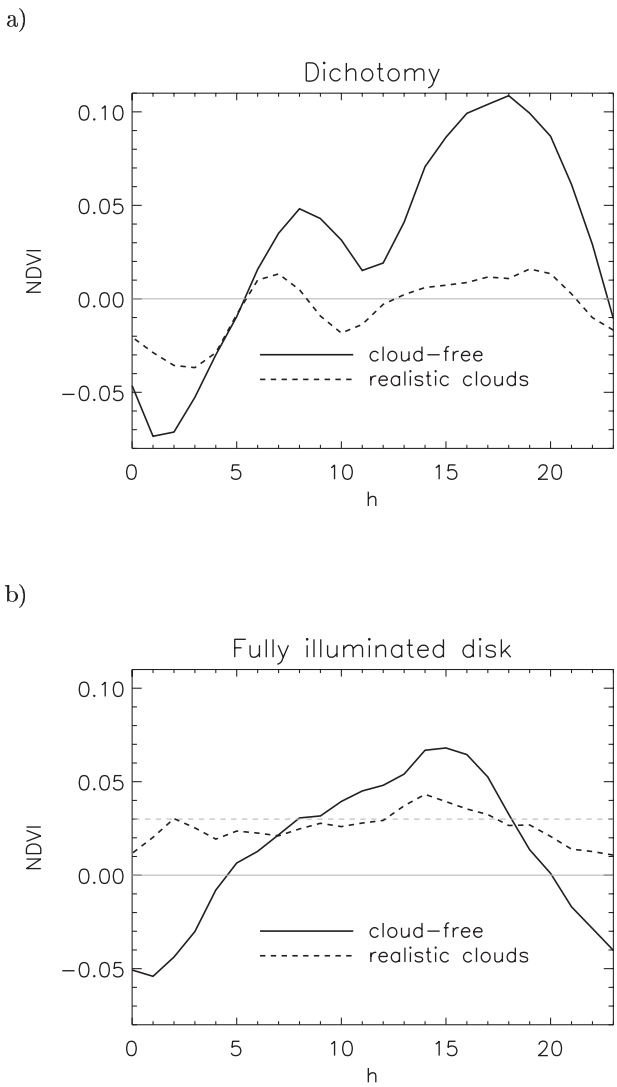

FIG. 11. NDVI for a cloud-free (solid lines) and cloudy rotating Earth (dashed lines): (a) dichotomies and (b) fully illuminated disks. Here we calculate the disk-averaged NDVI of our model using in Eq. 3 0.65–0.68 μm for the red and 0.75–0.8 μm for the NIR. The gray lines indicate the thresholds to discriminate for that phase the presence of the red-edge.

tribution of plankton to our simulation did not improve the fit between the data and the model.

DISCUSSION

We compared our light-curves in the VIS at dichotomy (Fig. 8b) with the simulations of Ford *et al*. (2001). In a cloud-free situation, we confirmed that the spectral range in the VIS/NIR with the largest photometric variability due to vegetation was between ~0.7 and 0.8 μm. We also confirmed that the rotation period was clearly observable if we observed the planet from an appropriate position with respect to the rotation axis. While the model of Ford *et al*. (2001) includes no explicit treatment of scattering or absorption by an atmosphere, our results confirmed many of their conclusions. For example, changes in ice cover increased the surface albedo by as much as 100% (Figs. 4 and 5a and c). We also confirmed the conclusion by Ford *et al*. (2001) that clouds tend to increase the overall brightness in the VIS/NIR when compared with the cloud-free case (Figs. 4, 5b and d, 6, 7a, and 8b).

However, our results indicated that when a comprehensive treatment of the surface and atmosphere were taken into account (see Figs. 8b and 9a), the maximum daily variation for a cloud-free case was about 50% (0.74–0.75 μm band) at dichotomy. We also found variations as large as 50% associated with cloud pattern variations on a typical day (Figs. 8b and 9b). This number decreased considerably as the phase was changed. Moreover, information about the surface rotation

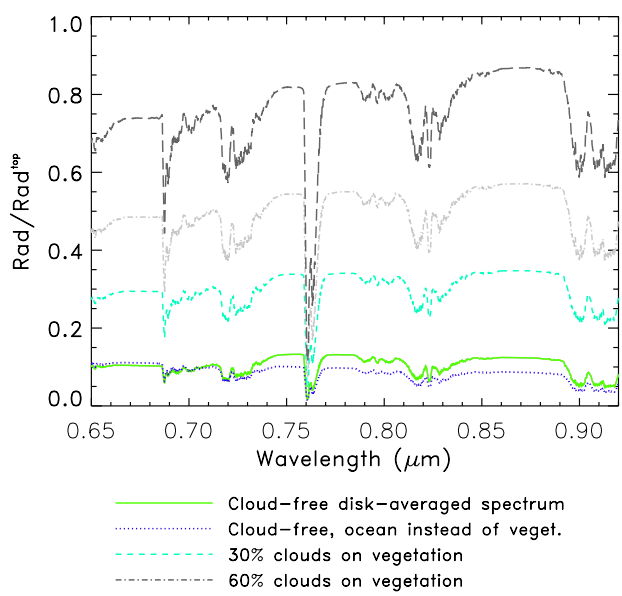

FIG. 12. Disk-averaged spectra in the optical of an increasing cloudy Earth. The clouds are simulated to be present only on the part of the surface covered by vegetation. This view angle gives ~40% vegetation cover (yellow-green solid line, cloud-free). As a comparison we include the same simulation with ocean 100% replacing the land vegetation (violet dotted line). Gray dashed line at the top, clouds are totally covering the vegetation. The other lines show intermediate situations (30% and 60% cloud cover).

period was lost when we included clouds (Fig. 8b). For an extrasolar terrestrial planet, these conclusions should be taken with some caveats, since they depend on the cloud pattern, the cloud microphysics, and the atmospheric general circulation on that planet. The planet Venus (the most Earthlike terrestrial planet in our solar system in size, mass, and solar distance) provides an extreme example. There, photochemical clouds completely hide the surface at VIS wavelengths and give the planet a very high albedo (~0.71). In addition, the ultraviolet features at the cloud tops have an apparent rotation period of only 4 days, while the solid body of the planet rotates only once every 242 days.

We also confirmed the hypothesis of Ford *et al*. (2001) that the diurnal rotation variation of an Earth-like planet might be lower in the MIR than in the VIS/NIR. As shown in Fig. 8, the temperature gradients between continents and oceans did not produce radiance variations as large as the surface albedo variations. This was due to the presence of a relatively thick atmosphere that acted to moderate the temperature excursions that would otherwise have occurred [see, for comparison, the Mars case (Tinetti *et al*., 2005)]. For cloudy cases in the MIR, the band-weighted integrated radiance was lower as a result of the lower effective temperature of the cloud deck. The amplitude of the variability was similar to that of the clear-sky case (~3% variation).

The earthshine data of Arnold *et al*. (2002) show that, while the atmosphere of the Earth is transparent enough to allow the vegetation signal to be measured, this signal is reduced by water vapor and oxygen absorption. They also found that a variable cloud cover and Earth phase may increase the difficulty of measuring the red-edge in earthshine. We confirmed these conclusions and used our model to explore in more detail how phases and cloud cover could influence the sensitivity of NDVI and provide more insight regarding how to discriminate the presence of vegetation. We found that certain types of clouds (mainly low and middle), because of their scattering properties, can act as a false positive when the Earth was observed at phases close to fully illuminated because those cloud types, like vegetation, produced a positive NDVI. The fully illuminated phase, however, will never be observed by TPF or similar missions.

Our model and disk- and diurnally averaged NDVI showed that the vegetation signal could be quite strong or completely hidden (Figs. 9–11). The problem of clouds obscuring vegetation on land is compounded by the fact that cloud cover may tend to favor vegetated areas (and vice versa). One reason for this is that vegetation promotes conductance of moisture from the soil to the atmosphere, and vegetation roughness promotes moisture convergence and, hence, cloud cover at the regional and continental scales (Dickinson, 1989; Friend and Kiang, 2005).

In this paper, we investigated the detectability of vegetation for only 1 day in the northern hemisphere summer. However, some of our results are likely to be valid for a larger fraction of an Earth year. From an inspection of AIRS and ISCCP time series of clouds, in fact, we know that cloud distributions on Earth vary most strongly in the latitudinal direction, and less so in the longitudinal direction. The equatorial region is characterized by a discontinuous band of convective clouds that migrate latitudinally with season and occur with higher frequency in the Western Pacific, Africa, and South America. The eastern Pacific, as well as other eastern boundary oceanic regions, is dominated by low stratus clouds through much of the year, though the frequency and coverage are modulated by seasonal changes. The mid-latitude storm track in the northern hemisphere is discontinuous and strongest over the Pacific and Atlantic Oceans and much stronger in the boreal winter than the summer. The storm track in the southern hemisphere is fairly continuous with less seasonal variability than in the northern hemisphere. The El Nino Southern Oscillation is a prominent feature that causes significant interannual variability in the spatial distribution and frequency of low, middle, and high clouds. Other elements of year-to-year variability in the atmospheric dynamical fields (*e.g.*, El Nino-Southern Oscillation) can have profound impacts on cloud cover from the perspective of the Earth's climate. From the TPF perspective, however, these modes of variability are negligible. The global variability in cloud cover induced by these modes is on the order of 1% or less globally (see: http://isccp.giss.nasa.gov/). As a result of some reorganization of cloud patterns, the partitioning of clouds over land versus ocean may change. This interannual variability in cloud cover over land may potentially impact the NDVI. Though the "detectability" of life signatures using NDVI and its sensitivity to detailed cloud variability on interannual time scales should be a subject of future

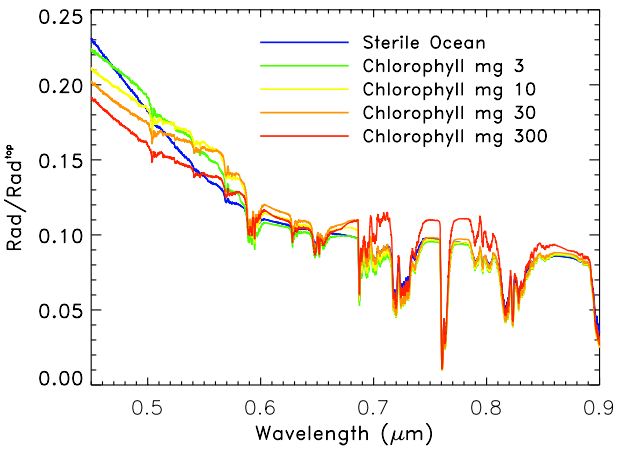

FIG. 13. Disk-averaged synthetic spectra of a cloud-free, predominantly ocean-view of the Earth (gibbous phase), with the concentration of plankton increasing from 0 (sterile ocean, blue line) to 300 mg/m^3 (extreme concentration, red line). For a present-day Earth the average concentration floats between 0.1 and 10 mg/m^3, with peaks up to 30 mg/m^3.

research, we expect that the results reported in this paper, which were produced using data collected during the northern hemisphere summer, will still be valid in the general case, especially when averaged over the diurnal cycle. Diurnal averaging effectively smooths out the large variability in cloud amount on time scales of hours. Different cloud patterns may change the NDVI curves calculated for disk-averaged cloudy spectra as a function of viewing geometry (Fig. 11). One would expect, for example, to have more vegetation covered by clouds in the Asian basin during the northern hemisphere summer than in the Amazonian forest, and vice versa, for the northern hemisphere winter season. Clouds are also likely to move northward or southward, depending on the season, over the African continent.

Other factors besides clouds that could obscure surface signatures include atmospheric gases. Oxygen—a potential biosignature produced by photosynthesis—and water are prerequisites for known life. If oxygen and water are present on another planet, they could obscure parts of an exoplanet's red-edge. The choice of red and NIR bands for our red-edge index (disk-averaged NDVI) were 0.65–0.68 μm for the red and 0.74–0.8 μm for the NIR. The band 0.65–0.68 μm for the red maximized, in the cloud-free case, the differences observed in the NIR band—hence the NDVI—since it lies just before the rise of the red-edge signature. At shorter wavelengths, the albedo increases for Rayleigh scattering, and, consequently, the amplitude of the NDVI progressively decreased. By contrast, in the fully illuminated cloudy case—the most critical one—the 0.65–0.68 μm band minimized the difference from the NIR band. We selected 0.74–0.8 μm for the NIR since the H_2O absorbance lines fell along the red-edge feature. By narrowing the selected band to 0.74–0.75 μm, which removes the oxygen band, the value of the NDVI could be magnified. However, this simulation does not improve the sensitivity of the NDVI, and it does not change our conclusions drawn from the existing model because the O_2 band is a small fraction of the overall NDVI bandwidth. We therefore used the broader band to be more flexible to potential shifts of the red-edge on another extrasolar planet (N.Y. Kiang *et al.*, manuscript submitted for publication). The NIR band at 0.74–0.8 μm, though, is subject to physiological variability for Earth photosynthetic organisms, whereas other possible choices, such as the 0.855–0.875 μm wavelength range, are fairly stable, even across mosses, lichens, and cyanobacteria. Unfortunately, the NDVI for those alternative band selections lost its sensitivity when the impact of the level of cloud cover on the strength of the vegetation signature was considered because clouds mimic the slope due to vegetation remarkably well in that band. For extrasolar terrestrial planet observations, clouds cannot be removed by improving the statistics of measurements. If TPF-C

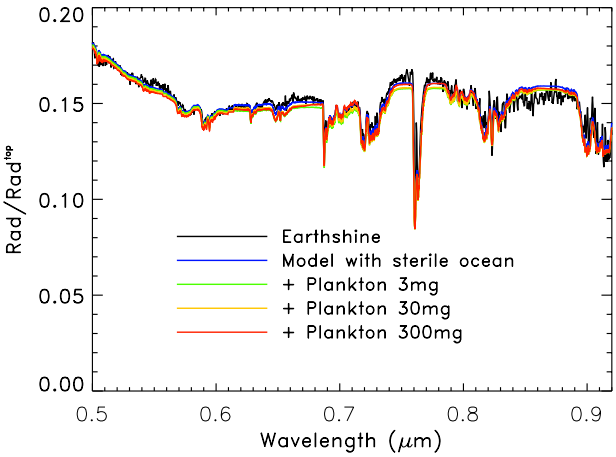

FIG. 14. Comparison between the earthshine spectrum of Woolf *et al.* (2002) (black line) and simulation for a sterile ocean (blue lines) with an increasing concentration of plankton.

could extend the wavelength range observed to at least the 1.4 μm band, a very useful channel for looking at the spectral signatures of clouds could be added.

Given potential TPF-C sensor bands at 0.65–0.68 μm and 0.74–0.80 μm, the red-edge detectability for the Earth whole disk requires at least 20% average diurnal land vegetation cover unobscured by clouds to achieve an index that is greater than 0. This means that a planet with a high percent of water over the surface could still reveal land surface photosynthetic activity. When clouds were included in our model, the threshold for discriminating the red-edge unambiguously was 0 for all of the phases most likely to be considered by TPF (see Table 1 and Fig. 11a).

With regard to marine vegetation, we investigated the detectability of plankton (Figs. 13 and 14). In Fig. 13, we show disk-averaged spectra of an ocean view of the Earth with an increasing concentration of plankton. As we already noted, this was an "optimistic" result since we assumed a clear sky and chose a particular viewing geometry and season in which plankton would be better detected (see: http://seawifs.gsfc.nasa.gov/SEAWIFS.html). When cloud realistic patterns were included in the simulations (Fig. 14), plankton was very hard to detect, even when present in high concentrations. Though the concentration of 300 mg of chlorophyll would not be realistic for present-day Earth, it is useful to illustrate how plankton could modify the spectral shape. In the case of an early Earth or an extrasolar terrestrial planet, higher plankton concentrations might be plausible.

Based on current knowledge of photosynthesis on Earth and of stellar evolution, Wolstencroft and Raven (2002) concluded that it is likely that photosynthesis can evolve on Earth-like planets in response to the same evolutionary factors that occurred on Earth. However, the chemical intermediates, catalysts, and the frequency of the photons activating the photosynthetic pigments may be different. Modeling of photosynthesis on Earth-like planets that orbit stars of different spectral types (Wolstencroft and Raven, 2002) shows that cooler stars, with maximum radiation output at longer wavelengths, may require more than the two light reactions used in oxygen-evolving photosynthesis on Earth; such photosynthesis would be limited by the attenuation of radiation by water. Detection of photosynthesis will be based on spectroscopy using, most likely, photosynthetic pigments that could have different absorption properties from those on Earth. Hence a red-edge like signal could be shifted to other wavelengths (Tinetti et al., 2006b).

CONCLUSIONS

We have used a three-dimensional comprehensive model that included a realistic surface, atmospheric properties, and clouds to simulate disk- and time-averaged spectra of the Earth.

Our results confirmed most of the conclusions of Ford *et al*. (2001). However, while the model of Ford *et al*. (2001) includes no explicit treatment of scattering or absorption by an atmosphere, our results indicated that, when a comprehensive treatment of the surface and atmosphere were taken into account, the maximum daily variation for a cloud-free case was about 50% (0.74–0.75 μm band) at dichotomy. We also observed variations as large as 50% within a typical day associated with variations in cloud patterns. We found that this number may decrease considerably as the phase changes.

We found that clouds modified the shapes and intensities of the spectrum and produced variations as large as 500% in the VIS for a completely overcast, half-illuminated planet and up to 50% in the MIR. Our disk-averaged spectra were remarkably sensitive to the illuminated phase in the VIS-NIR when clouds were present. Dramatic differences were observed for both albedo intensities and spectral shapes. This was attributed to changes in atmospheric pathlength above the clouds and the different relative position of the observer with respect to the Sun.

In cloud-free simulations, the red-edge biosignature should be detectable depending upon the instrumentation capabilities because, as we have shown, on a cloud-free Earth the red-edge can produce up to a 50% increase in albedo in the NIR. Though it will be harder to detect this signal when clouds are present, it will be feasible for the phases most likely to be detected by TPF. Plankton will be challenging to discriminate, as we demonstrated here for current Earth plankton abundances. Even in the case of a shallow ocean world with an order of magnitude greater plankton concentration, the signal in the disk-average was found to be far weaker than the land vegetation signal.

The dependence of cloudy disk-averaged spectra on phase may change for a planet with condensates and cloud microphysics different from Earth, and the red-edge, if present on such a planet, may be shifted as well. As a consequence, our results, tuned for the Earth case, may not be generalized to all terrestrial planets.

ACKNOWLEDGMENTS

We would like to thank Jim Kasting, Vijay Natraj, and Sky Rashby for reviewing the paper. We thank the two anonymous referees who helped to improve this paper. This material is based upon work performed by the NASA Astrobiology Institute's Virtual Planetary Laboratory Lead Team, supported by the National Aeronautics and Space Administration through the NASA Astrobiology Institute under Cooperative Agreement number CAN-00-OSS-01. Some of this work was performed by the Jet Propulsion Laboratory of the California Institute of Technology. G.T. is supported by an ESA external fellowship. M.T. is supported by a NASA Astrobiology Institute-National Research Council research associateship.

ABBREVIATIONS

AIRS, Atmospheric Infrared Sounder; ISCCP, International Satellite Cloud Climatology Project; MIR, mid-infrared; NDVI, normalized difference vegetation index; NIR, near-infrared; S/N, signal-to-noise ratio; TPF, Terrestrial Planet Finder; TPF-C, Terrestrial Planet Finder Coronagraph; TPF-I, Terrestrial Planet Finder Interferometer; VIS, visible.

REFERENCES

Arnold, L., Gillet, S., Lardière, O., Riaud, P., and Schneider, J. (2002) A test for the search for life on extrasolar planets: looking for the terrestrial vegetation signature in the Earthshine spectrum. *Astron. Astrophys*. 392(1), 231–237.

Arnold, L., Breon, F.-M., Brewer, S., Guiot, J., Jacquemoud, S., and Schneider, J. (2003) The green vegetation as a biosignatures on earth and Earth-like planets: POLDER data and earthshine observations. In *SF2A 2003*, edited by F. Combes, D. Barret, T. Contini, and L. Pagani, EdP Sciences, Les Ulis, France, p. 133.

Aumann, H.H., Gregorich, D., and Gaiser, S. (2005) AIRS hyper-spectral measurements for climate research: carbon dioxide and nitrous oxide effects. *Geophys. Res. Lett*. 32, L05806.

Beichman, C.A., Woolf, N.J., and Lindensmith, C.A., eds. (1999) *The Terrestrial Planet Finder (TPF)*, JPL Publication No. 99–3, Jet Propulsion Laboratory, Pasadena, CA. Available at: http://planetquest.jpl.nasa.gov/TPF/tpf_index.html.

Crisp, D. (1997) Absorption of sunlight by water vapor in cloudy conditions: a partial explanation for the cloud absorption anomaly. *Geophys. Res. Lett*. 24, 571–574.

Dickinson, R.E. (1989 Modeling the effects of Amazonian deforestation on regional surface climate: a review. *Agric. Forest Meteorol*. 47, 339–347.

Fishbein, E., Farmer, C.B., Granger, S.L., Gregorich, D.T., Gunson, M.R., Hannon, S.E., Hofstadter, M.D., Lee, S.-Y., and Leroy, S.S. (2003) Formulation and validation of simulated data for the Atmospheric Infrared Sounder (AIRS). *IEEE Trans. Geosci. Remote Sensing* 41(2), 314–329.

Ford, E.B., Seager, S., and Turner, E.L. (2001) Characterization of extrasolar terrestrial planets from diurnal photometric variability. *Nature* 412(6850), 885–887.

Friend, A.D. and Kiang, N.Y. (2005) Land surface model development for the GISS GCM: effects of improved canopy physiology on simulated climate. *J. Climate* 18(15), 2883–2902.

Fridlund, C.V.M. (2000) Darwin—the Infrared Space Interferometry Mission. *ESA Bull*. 103, 20–25. Available at: http://www.esa.int/esaSC/120382_index_0_m.html.

Gower, J., King, S., Yan, W., Borstad, G., and Brown, L. (2004) Use of the 709 nm band of MERIS to detect intense plankton blooms and other conditions in coastal waters. In *ESA SP-549: Proceedings of the MERIS User Workshop, 10–13 November 2003* [on CD-ROM], edited by H. Lacoste, ESA-ESRIN, Frascati, Italy, p. 27.1.

Kirk, J.T.O. (1983) *Light and Photosynthesis in Aquatic Ecosystems*, Cambridge University Press, Cambridge, UK.

Kuze, A. and Chance, K.V. (1994) Analysis of cloud top height and cloud coverage from satellites using the O_2 A and B bands. *J. Geophys. Res*. 99, 14481–14491.

Rossow, W.B. and Schiffer, R.A. (1999) Advances in understanding clouds from ISCCP. *Bull. Am. Meteor. Soc*. 80, 2261–2287.

Salomonson, V.V. and Toll, D.L. (1991) Execution phase (C/D) spectral band characteristics of the EOS moderate resolution imaging spectrometer-nadir (MODIS-N) facility instrument. *Adv. Space Res*. 11(3), 231–236.

Seager, S., Turner, E.L., Schafer, J., and Ford, E.B. (2005) Vegetation's red edge: a possible spectroscopic biosignature of extraterrestrial plants. *Astrobiology* 5(3), 372–390

Tinetti, G., Meadows, V.S., Crisp, D., Fong, W., Velusamy, T., and Snively, H. (2005) Disk-averaged synthetic spectra of Mars. *Astrobiology* 5(4), 461–481.

Tinetti, G., Meadows, V.S., Crisp, D., Fishbein, E., Turnbull, M., and Bibring, J.-P. (2006a) Detectability of planetary characteristics in disk-averaged spectra. I: The Earth model. *Astrobiology* 6(1), 34–47.

Tinetti, G., Rashby, S., and Yung, Y.L. (2006b) Detectability of red-edge–shifted vegetation on terrestrial planets orbiting M stars. *Astrophys. J.* 644(2), L129–L132.

Tucker, C.J. (1978) A comparison of satellite sensor bands for vegetation monitoring. *Photogrammetric Eng. Remote Sensing* 44(11), 1369–1380.

Wolstencroft, R.D. and Raven, J.A. (2002) Photosynthesis: likelihood of occurrence and possibility of detection on Earth-like planets. *Icarus* 157(2), 535–548.

Woolf, N.J., Smith, P.S., Traub, W.A., and Jucks, K.W. (2002) The spectrum of earthshine: a pale blue dot observed from the ground. *Astrophys. J.* 547(1), 430–433.

Address reprint requests to:
Giovanna Tinetti
Institut d'Astrophysique de Paris
98bis Boulevard Arago
Paris 75014, France

E-mail: tinetti@iap.fr, gtinetti@gmail.com

This article has been cited by:

1. P.G.J. Irwin, J.K. Barstow, N.E. Bowles, L.N. Fletcher, S. Aigrain, J.-M. Lee. 2014. The transit spectra of Earth and Jupiter. *Icarus* **242**, 172-187. [CrossRef]
2. S. Seager. 2014. The future of spectroscopic life detection on exoplanets. *Proceedings of the National Academy of Sciences* **111**, 12634-12640. [CrossRef]
3. Fujii Yuka, Kimura Jun, Dohm James, Ohtake Makiko. 2014. Geology and Photometric Variation of Solar System Bodies with Minor Atmospheres: Implications for Solid Exoplanets. *Astrobiology* **14**:9, 753-768. [Abstract] [Full Text HTML] [Full Text PDF] [Full Text PDF with Links]
4. E. Sanromá, E. Pallé, M. N. Parenteau, N. Y. Kiang, A. M. Gutiérrez-Navarro, R. López, P. Montañés-Rodríguez. 2014. CHARACTERIZING THE PURPLE EARTH: MODELING THE GLOBALLY INTEGRATED SPECTRAL VARIABILITY OF THE ARCHEAN EARTH. *The Astrophysical Journal* **780**, 52. [CrossRef]
5. Giovanna Tinetti, Thérèse Encrenaz, Athena Coustenis. 2013. Spectroscopy of planetary atmospheres in our Galaxy. *The Astronomy and Astrophysics Review* **21**. . [CrossRef]
6. M. Vasquez, F. Schreier, S. Gimeno García, D. Kitzmann, B. Patzer, H. Rauer, T. Trautmann. 2013. Infrared radiative transfer in atmospheres of Earth-like planets around F, G, K, and M stars. *Astronomy & Astrophysics* **557**, A46. [CrossRef]
7. E. Sanromá, E. Pallé, A. García Munõz. 2013. ON THE EFFECTS OF THE EVOLUTION OF MICROBIAL MATS AND LAND PLANTS ON THE EARTH AS A PLANET. PHOTOMETRIC AND SPECTROSCOPIC LIGHT CURVES OF PALEO-EARTHS. *The Astrophysical Journal* **766**:2, 133. [CrossRef]
8. T. Karalidi, D. M. Stam, J. W. Hovenier. 2012. Looking for the rainbow on exoplanets covered by liquid and icy water clouds. *Astronomy & Astrophysics* **548**, A90. [CrossRef]
9. T. Karalidi, D.M. Stam. 2012. Flux and polarisation signals of horizontally inhomogeneous exoplanets applied to Earth-like planets. *Astronomy & Astrophysics* . [CrossRef]
10. Yuka Fujii, Hajime Kawahara. 2012. MAPPING EARTH ANALOGS FROM PHOTOMETRIC VARIABILITY: SPIN-ORBIT TOMOGRAPHY FOR PLANETS IN INCLINED ORBITS. *The Astrophysical Journal* **755**, 101. [CrossRef]
11. Michael F. Sterzik, Stefano Bagnulo, Enric Palle. 2012. Biosignatures as revealed by spectropolarimetry of Earthshine. *Nature* **483**, 64-66. [CrossRef]
12. J.T. O'Malley-James, J.A. Raven, C.S. Cockell, J.S. Greaves. 2012. Life and Light: Exotic Photosynthesis in Binary and Multiple-Star Systems. *Astrobiology* **12**:2, 115-124. [Abstract] [Full Text HTML] [Full Text PDF] [Full Text PDF with Links]
13. E. Sanromá, E. Pallé. 2012. RECONSTRUCTING THE PHOTOMETRIC LIGHT CURVES OF EARTH AS A PLANET ALONG ITS HISTORY. *The Astrophysical Journal* **744**:2, 188. [CrossRef]
14. Timothy A. Livengood, L. Drake Deming, Michael F. A'Hearn, David Charbonneau, Tilak Hewagama, Carey M. Lisse, Lucy A. McFadden, Victoria S. Meadows, Tyler D. Robinson, Sara Seager, Dennis D. Wellnitz. 2011. Properties of an Earth-Like Planet Orbiting a Sun-Like Star: Earth Observed by the EPOXI Mission. *Astrobiology* **11**:9, 907-930. [Abstract] [Full Text HTML] [Full Text PDF] [Full Text PDF with Links]
15. Hajime Kawahara, Yuka Fujii. 2011. MAPPING CLOUDS AND TERRAIN OF EARTH-LIKE PLANETS FROM PHOTOMETRIC VARIABILITY: DEMONSTRATION WITH PLANETS IN FACE-ON ORBITS. *The Astrophysical Journal* **739**, L62. [CrossRef]
16. Yuka Fujii, Hajime Kawahara, Yasushi Suto, Satoru Fukuda, Teruyuki Nakajima, Timothy A. Livengood, Edwin L. Turner. 2011. COLORS OF A SECOND EARTH. II. EFFECTS OF CLOUDS ON PHOTOMETRIC CHARACTERIZATION OF EARTH-LIKE EXOPLANETS. *The Astrophysical Journal* **738**, 184. [CrossRef]
17. D. Kitzmann, A. B.C. Patzer, P. von Paris, M. Godolt, H. Rauer. 2011. Clouds in the atmospheres of extrasolar planets. III. Impact of low and high-level clouds on the reflection spectra of Earth-like planets. *Astronomy & Astrophysics* . [CrossRef]
18. D. Kitzmann, A. B. C. Patzer, P. von Paris, M. Godolt, H. Rauer. 2011. Clouds in the atmospheres of extrasolar planets. *Astronomy & Astrophysics* **531**, A62. [CrossRef]
19. Tyler D. Robinson, Victoria S. Meadows, David Crisp, Drake Deming, Michael F. A'Hearn, David Charbonneau, Timothy A. Livengood, Sara Seager, Richard K. Barry, Thomas Hearty, Tilak Hewagama, Carey M. Lisse, Lucy A. McFadden, Dennis D. Wellnitz. 2011. Earth as an Extrasolar Planet: Earth Model Validation Using EPOXI Earth Observations. *Astrobiology* **11**:5, 393-408. [Abstract] [Full Text HTML] [Full Text PDF] [Full Text PDF with Links]
20. Nicolas B. Cowan, Tyler Robinson, Timothy A. Livengood, Drake Deming, Eric Agol, Michael F. A'Hearn, David Charbonneau, Carey M. Lisse, Victoria S. Meadows, Sara Seager, Aomawa L. Shields, Dennis D. Wellnitz. 2011. ROTATIONAL

VARIABILITY OF EARTH'S POLAR REGIONS: IMPLICATIONS FOR DETECTING SNOWBALL PLANETS. *The Astrophysical Journal* **731**, 76. [CrossRef]

21. J.L. Grenfell, S. Gebauer, P. von Paris, M. Godolt, P. Hedelt, A.B.C. Patzer, B. Stracke, H. Rauer. 2011. Sensitivity of biomarkers to changes in chemical emissions in the Earth's Proterozoic atmosphere. *Icarus* **211**, 81-88. [CrossRef]
22. Christopher E. Doughty, Adam Wolf. 2010. Detecting Tree-like Multicellular Life on Extrasolar Planets. *Astrobiology* **10**:9, 869-879. [Abstract] [Full Text HTML] [Full Text PDF] [Full Text PDF with Links]
23. Tyler D. Robinson, Victoria S. Meadows, David Crisp. 2010. DETECTING OCEANS ON EXTRASOLAR PLANETS USING THE GLINT EFFECT. *The Astrophysical Journal* **721**, L67-L71. [CrossRef]
24. Hajime Kawahara, Yuka Fujii. 2010. GLOBAL MAPPING OF EARTH-LIKE EXOPLANETS FROM SCATTERED LIGHT CURVES. *The Astrophysical Journal* **720**, 1333-1350. [CrossRef]
25. Yuka Fujii, Hajime Kawahara, Yasushi Suto, Atsushi Taruya, Satoru Fukuda, Teruyuki Nakajima, Edwin L. Turner. 2010. COLORS OF A SECOND EARTH: ESTIMATING THE FRACTIONAL AREAS OF OCEAN, LAND, AND VEGETATION OF EARTH-LIKE EXOPLANETS. *The Astrophysical Journal* **715**, 866-880. [CrossRef]
26. E. Pallé. 2010. Earthshine observations of an inhabited planet. *EAS Publications Series* **41**, 505-516. [CrossRef]
27. P. H. H. Oakley, W. Cash. 2009. CONSTRUCTION OF AN EARTH MODEL: ANALYSIS OF EXOPLANET LIGHT CURVES AND MAPPING THE NEXT EARTH WITH THE NEW WORLDS OBSERVER. *The Astrophysical Journal* **700**, 1428-1439. [CrossRef]
28. Nicolas B. Cowan, Eric Agol, Victoria S. Meadows, Tyler Robinson, Timothy A. Livengood, Drake Deming, Carey M. Lisse, Michael F. A'Hearn, Dennis D. Wellnitz, Sara Seager, David Charbonneau. 2009. ALIEN MAPS OF AN OCEAN-BEARING WORLD. *The Astrophysical Journal* **700**, 915-923. [CrossRef]
29. Sally V. Langford, J. Stuart B. Wyithe, Edwin L. Turner. 2009. Photometric Variability in Earthshine Observations. *Astrobiology* **9**:3, 305-310. [Abstract] [Full Text PDF] [Full Text PDF with Links]
30. Thomas Hearty, Inseok Song, Sam Kim, Giovanna Tinetti. 2009. MID-INFRARED PROPERTIES OF DISK AVERAGED OBSERVATIONS OF EARTH WITH AIRS. *The Astrophysical Journal* **693**, 1763-1774. [CrossRef]
31. C.S. Cockell, A. Léger, M. Fridlund, T.M. Herbst, L. Kaltenegger, O. Absil, C. Beichman, W. Benz, M. Blanc, A. Brack, A. Chelli, L. Colangeli, H. Cottin, F. Coudé du Foresto, W.C. Danchi, D. Defrère, J.-W. den Herder, C. Eiroa, J. Greaves, T. Henning, K.J. Johnston, H. Jones, L. Labadie, H. Lammer, R. Launhardt, P. Lawson, O.P. Lay, J.-M. LeDuigou, R. Liseau, F. Malbet, S.R. Martin, D. Mawet, D. Mourard, C. Moutou, L.M. Mugnier, M. Ollivier, F. Paresce, A. Quirrenbach, Y.D. Rabbia, J.A. Raven, H.J.A. Rottgering, D. Rouan, N.C. Santos, F. Selsis, E. Serabyn, H. Shibai, M. Tamura, E. Thiébaut, F. Westall, G.J. White. 2009. Darwin—A Mission to Detect and Search for Life on Extrasolar Planets. *Astrobiology* **9**:1, 1-22. [Abstract] [Full Text PDF] [Full Text PDF with Links]
32. Rory Barnes, Sean N. Raymond, Brian Jackson, Richard Greenberg. 2008. Tides and the Evolution of Planetary Habitability. *Astrobiology* **8**:3, 557-568. [Abstract] [Full Text PDF] [Full Text PDF with Links]
33. D. M. Stam. 2008. Spectropolarimetric signatures of Earth-like extrasolar planets. *Astronomy and Astrophysics* **482**, 989-1007. [CrossRef]
34. Luc Arnold. 2008. Earthshine Observation of Vegetation and Implication for Life Detection on Other Planets. *Space Science Reviews* **135**, 323-333. [CrossRef]
35. A. Belu, E. Thiébaut, M. Ollivier, G. Lagache, F. Selsis, F. Vakili. 2007. A scene model of exosolar systems for use in planetary detection and characterisation simulations. *Astronomy and Astrophysics* **476**, 1005-1018. [CrossRef]
36. Jill C. Tarter, Peter R. Backus, Rocco L. Mancinelli, Jonathan M. Aurnou, Dana E. Backman, Gibor S. Basri, Alan P. Boss, Andrew Clarke, Drake Deming, Laurance R. Doyle, Eric D. Feigelson, Friedmann Freund, David H. Grinspoon, Robert M. Haberle, Steven A. Hauck II, Martin J. Heath, Todd J. Henry, Jeffery L. Hollingsworth, Manoj M. Joshi, Steven Kilston, Michael C. Liu, Eric Meikle, I. Neill Reid, Lynn J. Rothschild, John Scalo, Antigona Segura, Carol M. Tang, James M. Tiedje, Margaret C. Turnbull, Lucianne M. Walkowicz, Arthur L. Weber, Richard E. Young. 2007. A Reappraisal of The Habitability of Planets around M Dwarf Stars. *Astrobiology* **7**:1, 30-65. [Abstract] [Full Text PDF] [Full Text PDF with Links]
37. Nancy Y. Kiang, Antígona Segura, Giovanna Tinetti, Govindjee, Robert E. Blankenship, Martin Cohen, Janet Siefert, David Crisp, Victoria S. Meadows. 2007. Spectral Signatures of Photosynthesis. II. Coevolution with Other Stars And The Atmosphere on Extrasolar Worlds. *Astrobiology* **7**:1, 252-274. [Abstract] [Full Text PDF] [Full Text PDF with Links]
38. John Scalo, Lisa Kaltenegger, Antígona Segura, Malcolm Fridlund, Ignasi Ribas, Yu. N. Kulikov, John L. Grenfell, Heike Rauer, Petra Odert, Martin Leitzinger, F. Selsis, Maxim L. Khodachenko, Carlos Eiroa, Jim Kasting, Helmut Lammer. 2007. M Stars as Targets for Terrestrial Exoplanet Searches And Biosignature Detection. *Astrobiology* **7**:1, 85-166. [Abstract] [Full Text PDF] [Full Text PDF with Links]